Ground-Based Urban Channel Characteristics for Two Public Safety Frequency Bands[1]

David W. Matolak[α], *Senior Member, IEEE*, Kate A. Remley[β], *Senior Member, IEEE, IEEE,* Camillo Gentile[γ], *Member, IEEE,* Christopher L. Holloway[β], *Senior Member,* Qiong Wu[α], Qian Zhang[α]

Abstract

We report on ground-based wireless channel characteristics for an urban environment in two public safety bands. Results are based upon measurements taken in Denver in June 2009. The public safety bands we investigated are the 700 MHz and 4.9 GHz bands, both planned for public safety and "emergency responder" applications. Measurements employed a vector network analyzer, from which both path loss and delay dispersion characteristics were obtained for link distances up to approximately 100 m. Log-distance models for path loss are presented, and proposed dispersive channel models are also described. By mounting the transmitter on a positioner, we introduced spatial diversity into the measurement system which enabled analyzing the dispersion characteristics of the angle-of-departure as well.

α Ohio University, School of Electrical Engineering & Computer Science, Athens, OH, 45701 USA (email matolak@ohiou.edu)

β National Institute of Standards & Technology, Dept. of Commerce, Electromagnetics Division, Boulder, CO, 80305 USA (email: kate.remley@nist.gov)

γ National Institute of Standards & Technology, Dept. of Commerce, Information Technology Laboratory, Gaithersburg, MD, 20899 USA (email: camillo.gentile@nist.gov)

I. Introduction

Communications for public safety authorities are seeing increased attention [1], [2]. This is due in part to increased awareness of the need for effective communications for so-called “first responders” during emergency events. In addition, new spectral allocations have been granted for public safety use, so public safety communities are working on how to best use these new bands. Several bands in the 700 MHz spectrum, formerly allocated to television broadcast, have been re-allocated to public safety nationwide, and a band in the 4900 MHz spectrum has also been recently allocated. In the 700 MHz band, two 12-MHz blocks are available from 764-776 MHz and 794-806 MHz, whereas in the 4900 MHz band, 50 MHz is available from 4940-4990 MHz.

Public safety communications have traditionally been “narrowband,” with voice the primary service. Channel allocations of 6.25, 12, and 25 kHz have been used for many years. The use of new, wider band services has been gaining popularity for applications such as video, geolocation, etc., and this has initiated development of wider-band air interface standards, such as the so-called P34 standard originally developed by the Association of Public Safety Communications Officials (APCO), now under the Telecommunications Industries Association (TIA) [3]. With the tremendous growth of wireless local and metropolitan area networks using the IEEE 802.11 and 802.16 (WiMAX, [4]) standard technologies, as well as cellular technologies, the public safety community is likely en-route to employ one or more of these technologies for reasons of reliability and economy. Typical values of occupied signal bandwidths for these technologies are 1.25, 5, 10, and 20 MHz.

Deployments for public safety communications have traditionally been of the “single-cell” or “dispatch” variety, where mobile users connect to a single base station that covers a wide area. For first responder events, new types of deployments, called the jurisdictional area network (JAN) and incident area network (IAN) are in the process of being deployed [1]. The JAN may

operate as a single- or multi-cell system over a wide area (e.g., city wide), whereas the IAN can operate as an ad hoc network, set up temporarily to provide communication services for first responders during an emergency event. Typical IAN environments will include urban settings, outdoor-outdoor, outdoor-indoor, and possibly indoor-indoor. In some scenarios, these systems will be ad hoc, and large, elevated base stations will not be deployable. Hence communication will be ground-based, or "peer-to-peer" (P2P), with low-elevation antennas communicating with mobile units, and mobile units communicating with each other. Our definition of ground-based (and P2P) here means just this: low elevation (primarily pedestrian height) antennas, with typically low (pedestrian) mobile velocities.

For any wireless communication system to operate reliably, knowledge of the channel characteristics is vital [5]. Key channel characteristics that influence selection of signaling parameters include delay dispersion, frequency coherence, Doppler spread, and temporal correlation. Knowledge of these characteristics enables optimal selection of transmission parameters (e.g., subcarrier bandwidth and symbol rate), as well as design parameters for remedial measures to counteract channel effects (e.g., equalization and diversity) [6]. Public safety communication systems in the 700- and 4900-MHz bands are yet to be widely deployed, so characterization of the wireless channels in these bands for first responder environments is presently needed. The Department of Justice Community-Oriented Policing Services (COPS) program has funded NIST's Public Safety Communications Research Laboratory for several efforts in this area, including work described in [7]-[9]. The urban channel characterization that is the subject of this paper is a continuation of this work.

Wireless channels for many environments have been characterized for numerous systems and in multiple frequency bands, with perhaps the cellular channel seeing the most attention, for

example [10], [11]. Indoor channels have also been characterized [12], as have other settings such as vehicle-to-vehicle [13]. Ground-based or P2P channels have seen much less attention. Path loss in UHF bands for ground-based urban channels was reported in [14]. Much work has also appeared on performance of ad hoc and cooperative communications in P2P settings, but this typically addresses aspects of network algorithm design and nearly universally employs conventional non-dispersive channel models. For example, [15] assumes Nakagami fading, and [16] assumes Rayleigh fading, and both these (and most other) references on P2P communications assume frequency *non*-selective fading, and hence do not address channel delay dispersion. Additionally, few references focus on bands near the 700-800 MHz band, and for those that do, results always pertain to a cellular-like deployment with one elevated antenna, e.g., [17], [18]. Similarly, although a large amount of work has been conducted for measuring and modeling channels in the 5 GHz band, e.g., [19], [20], very little has appeared for the ground-based environment. For brevity, we have provided only representative citations to the vast literature in the area of urban wireless channel measurements and models. Our work described here fills a gap by presenting channel measurement and modeling results for ground-based urban channels in the 700- and 4900 MHz public safety frequency bands.

The remainder of this paper is organized as follows. Section II describes the urban environment and measurement parameters. Section III presents delay dispersion characteristics for both line of sight (LOS) and non-LOS (NLOS) conditions, and also provides estimates of bandwidths for which frequency correlation reaches values of 0.5. We also describe a path loss model based on our data. In Section IV we provide a summary of some of the channel's spatial characteristics, and Section V provides conclusions.

II. Measurement Summary

The measurements were taken outdoors in downtown Denver, in the financial district, on Saturday June 20, 2009. This area contains many large (over 20 storey) buildings. Figure 1 shows an illustration of the test area constructed from a Google map view. The test area was the block between 17th and 18th Streets, and between Welton Street and Glenarm Place. Street widths are on the order of 20 m. Three transmitter (Tx) locations and eleven receiver (Rx) locations were used, for a total of 33 Tx-Rx location pairs. Figure 1 also shows a photograph of the two receiver antennas located at position R5 on the corner of Welton and 17th Streets. Line of sight link distances ranged from 10 m to 80 m. Non-LOS link distances are described in one of two ways:

(1) by an "L-shape," with the first distance d_1 corresponding to the LOS distance from the Tx to a corner (e.g., T_1 to R_5 in Fig. 1), and the second distance d_2 corresponding to the distance from the corner to the Rx (e.g., R_5 to R_9 in Fig. 1); or,

(2) by a "U-shape," with d_1 as previously defined, d_2 the corner to corner distance, and d_3 defined as the final distance from the second corner to the Rx (e.g., R_9 to R_{10} in Fig. 1).

Table I lists all these distances.[2] This approach for specifying distances in the urban environment has been used by others, for example [14].

The measurements employed a vector network analyzer (VNA), which measures the channel transfer function $H(f)$ as the scattering parameter S_{ij}, with transmission from port j to port i. The transfer function is measured relative to a reference to calibrate out antenna and system frequency variation. Our four-port VNA enabled us to connect simultaneously to separate antennas for the 700 MHz and 4900 MHz bands. Omni-directional antennas were used for both bands; a discone for 700 MHz, and a monopole for 4900 MHz, both vertically polarized.

[2] Note there is no Rx1 data; this Rx location was indoors, and those measured results are not included in this paper.

Identical antennas were used at Tx and Rx. A synchronized fiber-optic link between Rx antennas and VNA Rx port enabled us to attain link distances up to 200 m. Figure 2 illustrates the VNA setup. The Tx antennas were set on a cart, and mounted to a "positioner." The positioner is a motor-controlled two-arm device that enabled us to move the Tx antennas precisely in a Cartesian coordinate plane parallel to the ground. The positioner range is 0.5 m by 0.5 m. The Rx antennas were mounted on tripods, and were moved manually from location to location. All antenna heights were approximately 1.6 m above the ground (to top of antenna).

For each band, we measured *H(f)* twice at each of the nine Tx antenna positions (for each physical Tx-Rx location pair), yielding 18 transfer functions per Tx-Rx location pair. The nine Tx antenna positions corresponded to nine points on the Cartesian grid of the positioner, with separation between each point equal to 25 cm in both dimensions. Figure 3 shows a plan view diagram of the positioner, with the nine individual antenna positions labeled P1-P9. With 33 Tx-Rx pair combinations, a total of 18×33=594 transfer functions was collected. Bandwidths of *H(f)* for both bands were set to 100 MHz, with frequency resolution 1 MHz (enabling a 1μs maximum delay), but strong interferers in the lower part of the 700 MHz band reduced that usable bandwidth to 75 MHz. Our transfer functions thus covered the 725-800 MHz and 4.9-5 GHz frequency bands.

For much of the time during measurements, only pedestrian motion was present, although automobile traffic increased as the day progressed. Traffic around the block was "stop and go," since stoplights were present at all intersections. Auto speeds were as large as approximately 10 m/s, which for single-scattering yields a maximum Doppler frequency at 5 GHz of $f_d=vf/c=10(5\times10^9)/3\times10^8\cong167$ Hz [5]. This yields a minimum channel coherence time of approximately $t_{c,min}\cong1/f_d=6$ ms for the 4900 MHz band. The same maximum velocity yields a

minimum coherence time of approximately 37 ms for the upper end of the 700 MHz band. With each VNA sweep across the band taking approximately 2 ms, the channel can be considered statistically stationary for each measured *H(f)*. With our measurement procedure, we were unable to measure fading dynamics. One might conjecture that with sufficiently rich scattering, fading could be modeled as Rayleigh, but this is a subject for future work.

III. Delay Spread, Path Loss, & Frequency Correlation

A. Delay Spread

Baseband (complex envelope) channel impulse responses (CIRs) were computed from the bandpass transfer functions as follows. First, transfer functions were windowed using a Hamming window to reduced delay-domain sidelobes. This technique is often employed with VNA measurements, for example [21]. Then the windowed transfer functions were inverse Fourier-transformed to obtain bandpass CIRs. These bandpass CIRs were then downconverted, and low-pass filtered using a 5th-order elliptic filter to suppress the double frequency components. For a CIR denoted $h(\tau, t_i)$, the corresponding i^{th} power delay profile (PDP) was computed as $P_i(\tau)=|h(\tau, t_i)|^2$. The CIR $h(\tau, t_i)$ represents the channel output at time t_i due to an impulse input at time $t_i-\tau$, and is given by [5]

$$h(\tau, t_i) = \sum_{k=1}^{L_{pi}} \alpha_{ki} e^{j\phi_{ki}} \delta(\tau - \tau_{ki}), \qquad (1)$$

where i indexes the i^{th} PDP, L_{pi} is the number of multipath components in the i^{th} PDP, and the amplitude and phase of the k^{th} multipath component (MPC) in the i^{th} PDP are α_{ki} and ϕ_{ki}, respectively. The δ is a Dirac delta, and τ_{ki} represents the delay of the k^{th} MPC of the i^{th} PDP.

Generally, α_{ki} and ϕ_{ki} are functions of time, but for each PDP in our case they can be considered constants. The PDP $P_i(\tau)$ can be expressed as

$$P_i(\tau) = \sum_{k=1}^{L_i} |\alpha_{ki}|^2 \, \delta(\tau - \tau_{ki}) . \quad (2)$$

In order to separate actual MPCs from noise, we also gathered pure noise transfer functions, denoted $N(f)$. These were obtained with the VNA transmit ports terminated in matched loads, so the Rx antennas received "ambient" noise only. From the $N(f)$ transfer functions, we computed complex baseband time delay domain noise samples. The noise samples were judged Gaussian by computing the Kullback-Leibler divergence D_{KL} [22], a goodness-of-fit measure for probability density functions. If D_{KL} equals zero, the fit to the Gaussian density is perfect, and as D_{KL} increases, the goodness of the fit decreases. Values of D_{KL} were always less than 0.06, and typically $D_{KL}<0.02$, indicating that the noise can be considered Gaussian.

We then set a noise threshold using the algorithm in [10], based upon the measured noise variance, such that the false alarm probability was 1 in 100 PDPs. All PDP samples below the noise threshold were discarded, and the false alarm probability means that for each sample in $P_i(\tau)$, the probability of mistaking a noise component for a multipath component was 0.01, or 1 noise sample mistaken for an MPC per 100 PDPs. Figure 4 shows typical PDPs for LOS and NLOS conditions for the 700 MHz band, and Figure 5 is an analogous figure for the 4900 MHz band. Note that all PDPs were normalized and delay-aligned by time-shifting back by the estimated direct-path delay, which was based upon the distances in Table I. In addition, we truncated all PDPs after collecting the first 99% of the PDP energy. In Figures 4 and 5, a dynamic range is also indicated. We define the dynamic range as the difference in dB between the PDP peak and the noise threshold. Mean dynamic ranges were above 18 dB for NLOS cases,

and above 39 dB for LOS cases. Several PDPs had dynamic range less than 10 dB, and these were judged as having too low a signal-to-noise ratio, and were hence discarded.

The average PDPs, computed over all PDPs for the given case (LOS or NLOS) and band, are shown in Figures 6 and 7. As can be seen, the average PDPs look similar for the two bands. Table II provides delay spread statistics for both cases and bands. The root-mean square delay spread (RMS-DS) is widely used as the definitive measure of delay dispersion. It is the square-root of the second central moment of the PDP [5]. Another delay spread measure that is sometimes used is the delay window [23]. The delay window is the duration that contains x% of the CIR energy, and this is denoted $W_{\tau,x}$; Table II lists average PDP delay windows for x=90% energy. To determine $W_{\tau,x}$ we use a symmetric window that finds the "middle" x% energy. That is, for our example with x=90, the delay window neglects the earliest 5% and the latest 5% of the CIR energy. The last delay domain dispersion measure that we list is the delay interval [23]. The delay interval $I_{\tau,X}$ is defined as the duration of the CIR containing all impulses above X dB down from the largest impulse.

As expected, NLOS delay spreads are substantially larger than those for LOS cases. Also as expected, delay spreads generally increase with link distance [24]. The 4900 MHz band delay spread values are also slightly larger than those for the 700 MHz band. This relationship does not always hold: delay spreads generally (but not always) decreased with frequency in [25], [26], but it is not clear if signal to noise ratio and dynamic range were equal in all bands in the results of [25] and [26]. This means that comparison of delay spread trends may not be completely fair. This holds true in our case as well: since we used an external amplifier at the transmit end of the VNA for the 4900 MHz band, the 4900 MHz dynamic ranges were generally larger than those for the 700 MHz band: mean values of dynamic range were 38 dB for the 4900 MHz band and

28 dB for the 700 MHz band. This can account for some of the larger delay spreads we observed at 4900 MHz. In addition, results in [25] and [26] were not for ground-based settings.

Since our measurements spanned several hours, the propagation conditions did not remain constant; conditions also of course change with Tx-Rx locations. This can be quantified in the delay domain by using "instantaneous" delay spread measures [27]. Essentially, we compute the delay spread measures for *each* PDP individually. We can then collect statistics on these values over the sets of PDPs to quantify the range of variation of the delay spread measures. Figures 8 and 9 show histograms of instantaneous RMS-DS for the two bands. These plots show the expected result that NLOS delay spreads are larger than those for LOS, and that the range of delay spreads is a significant fraction of the mean. We can quantify this range via the coefficient of variation $CV=\sigma_{RMS\text{-}DS}/\mu_{RMS\text{-}DS}$, the ratio of delay spread standard deviation to delay spread mean: values of CV here are 0.27-0.34 for NLOS and 0.49-0.56 for LOS cases. Table III provides additional statistics on the instantaneous RMS-DS, and Table IV shows analogous statistics for the 90% energy delay window $W_{\tau,90}$ and 25 dB delay interval $I_{\tau,25}$. As expected for this ground-based, short-range setting, RMS-DS values are much smaller than those for cellular: for example the COST207 typical urban cellular channel has RMS-DS~1μs [28]. Our delay spread values are also substantially smaller than those in [25], [26], in which median delay spreads for their (elevated-antenna) measurements range from 300-700 ns in frequency bands from 430 MHz to 6 GHz.

For creating channel models, one would like to know the number of MPCs present. We used the algorithm in [29] to estimate the number of MPCs, denoted L_p, in each transfer function. The modified MUSIC algorithm of [29] uses the minimum description length criterion [30] to determine the number of MPCs, based upon modeling the time-invariant transfer function as a

harmonic function of delay. That is, the Fourier transform of the i^{th} CIR is viewed as a function of delay τ, at our given set of measured frequency points $\{f_{ki}\}$, thus, directly from (1) and [30, equations (2), (3)], we have,

$$H(f,t_i)=\sum_{k=1}^{L_{pi}}\alpha_{ki}e^{j\phi_{ki}}\exp(-j2\pi f\tau_{ki})\rightarrow H(\tau,t_i)=\sum_{k=1}^{L_{pi}}\alpha_{ki}e^{j\phi_{ki}}\exp(-j2\pi f_{ki}\tau), \quad (3)$$

and this representation enables use of MUSIC on this dual function for estimating the discrete delays. Summary statistics for the number of MPCs are presented in Table V. These statistics count the number of components within a 25 dB threshold of the peak component in each PDP—we truncated each PDP before applying the MUSIC algorithm. We employed this threshold since most communication systems typically do not operate at signal to noise ratios much larger than this value, and hence models that retain only the largest components are common, e.g., those within a 20 dB threshold in [31]. Typically one would expect the NLOS cases to have a substantially larger number of MPCs than the LOS cases, but the NLOS numbers are only slightly larger here. We attribute this to the lower dynamic range of the NLOS PDPs.

The distribution of the number of MPCs L_p was found to be best fit by a modified uniform distribution. Specifically, let L_{pmin} equal the minimum value of L_p, and L_{pmax} its maximum value (see Table V). We denote the probability mass function for L_p by $Pr(L_p=m)$, with integer $m\in\{L_{pmin}, L_{pmin}+1, \ldots L_{pmax}\}$. The mass function has weight p_0 at L_{pmax}, and is uniform with weight equal to $(1-p_0)/(L_{pmax}-L_{pmin})$ from L_{pmin} to L_{pmax}-1, i.e.,

$$\Pr(L_p=m)=\begin{cases}\dfrac{1-p_0}{L_{p\max}-L_{p\min}}, & m=L_{p\min}, L_{p\min}+1, \ldots L_{p\max}\text{-}1\\ p_0, & m=L_{p\max}\end{cases}. \quad (4)$$

Values of p_0 for the probability mass functions are also listed in Table V. As seen from Table V, 18-21 MPCs suffice for the 100 MHz band channel at 4900 MHz, and 11-14 MPCs suffice for

the 75 MHz band channel at 700 MHz. For construction of channel models for smaller values of bandwidths, MPCs can be combined, as in [20] or [32].

The distribution of the powers in these MPCs was obtained by fitting to the average PDPs of Figures 6 and 7. For these cases, we employed the following models:

$$P_{\tau,LOS}(\tau) = c_0 \exp(-c_1\tau) \tag{5}$$

$$P_{\tau,NLOS}(\tau) = \sum_{k=1}^{N_c} b_{k0} \exp[-b_{k1}(\tau - \tau_k)] \tag{6}$$

where N_c=3 is the number of clusters of multipath components for the NLOS case. The use of clusters is common in channel models for other settings as well, for example the indoor setting in [12], and the outdoor macrocell setting in [31]. Our clusters were based upon visual observation of the average PDPs. They are more well-defined for the 700 MHz band data—the 4900 MHz band clusters tend to overlap more substantially (see Figures 6, 7). The model coefficients are given in Table VI, and the first cluster delay τ_1=0.

For the delays of the MPCs within clusters, other researchers have employed randomly distributed delays, for example Poisson in [12], or for ultrawideband channels, uniformly distributed delays [33], or Weibull distributed delays [34], [35]. If we base the delay distribution upon the average PDPs, uniform distributions of delays fit the LOS cases, in intervals [0, 500 ns) for the 700 MHz band and [0, 550 ns) for the 4900 MHz band. The average PDPs for the NLOS cases could also be fit with uniformly distributed delays. Yet better models for the delay distributions were derived by collecting statistics on delays over *all* the measured PDPs. The results of this were that the LOS cases were best fit by an exponential distribution of delays, and the NLOS cases were best fit by a Weibull distribution [36] of delays. Specifically, the MPC delay probability density functions are as follows:

$$p_{\tau,LOS}(\tau) = \exp(-\tau / v) / v \tag{7}$$

$$p_{\tau,NLOS}(\tau) = \frac{\beta}{a^{\beta}} \tau^{\beta-1} \exp\left[-\left(\frac{\tau}{a} \right)^{\beta} \right] \tag{8}$$

where in the Weibull density of (8), β is the shape factor, and $a = \sqrt{\Omega / \Gamma[(2/\beta)+1]}$ is a scale parameter with $\Omega = E(\tau^2)$ the second moment, and Γ is the gamma function. Parameter values for these MPC delay probability density functions are given in Table VII.

Finally, note that in other models ([12], [31]), for simplicity, the decay constants b_{kl} of (6) for the decays within each cluster are assumed identical. As with our results here though, this is not always true: some ultrawideband models described in [33] employ different values of decay constants per cluster. If desired for simplicity, one could of course select a single value of decay constant from our models as well.

B. Path Loss

With a known transmit power, reference measurement, and accurate calibration, our VNA measurements can also be used to estimate propagation path loss. For each Tx-Rx location pair, we have 18 path loss measurements. These correspond to three groups of six measurements on our Cartesian positioner: group one is the six measurements (two measurements at each of the three positioner points) at distance d, group two the six measurements at distance d+0.25 m, and group three the six measurements at d+0.5 m. (Recall we have nine points on our Cartesian grid for each Tx antenna location, and at each point we collected two transfer functions—see Figure 3.)

To attempt to average out the effects of small scale (multipath) fading, we estimated the path loss as the difference between the known transmit power at band center (equal to the power

at any frequency in the band) and the average of the magnitude-squared of the received transfer function, with the average taken across all frequency points in the band (75 MHz for the 700 MHz band, and 100 MHz for the 4900 MHz band).

Figure 10 shows a plot of excess path loss in dB versus *10log(distance/d_0)* for the 700 MHz band, transmitter location T1, where d_0=4 m is the reference distance. This reference distance was also used for the 4900 MHz band. Reference path loss measurements were made at the NIST open area test site in Boulder, CO which closely emulated free-space conditions. Linear fits on the log-log scale are also shown in the figure. These are least-squares fits, and for the LOS case, these fits correspond to the following path loss model:

$$L_{LOS}(d) = L(d_0) + 10n_{LOS}\log(d/d_0) + X_{LOS}, \quad (9)$$

where n_{LOS} is the propagation path loss exponent, and X_{LOS} is a zero-mean Gaussian random variable with standard deviation σ_X dB. For NLOS L-shaped paths we use

$$L_{NLOS}(d_1, d_2) = \tilde{L}_{LOS}(d_1) + 10n_{NLOS}\log(d_2/d_1) + L_c + X_{NLOS}, \quad (10)$$

where n_{NLOS} and X_{NLOS} are analogous to the LOS parameter definitions, distances d_1 and d_2 correspond to L-shaped path distances (see Section II), and $\tilde{L}_{LOS}(d_1) = L_{LOS}(d_1) - X_{LOS}$, so that we do not apply the Gaussian random variable twice for the NLOS path loss. The parameter L_c is the "corner loss" added to the LOS path loss at distance d_1; this loss term was also used in [14]. The corner loss represents the "step" discontinuity amount between the LOS and NLOS fits; see Figure 10. The intercept value $L(d_0)$ is equal to the free-space value at band center for both bands, i.e., $L_{700MHz}(d_0)$=42 dB, and $L_{4900MHz}(d_0)$=58 dB. We define excess path loss here as $L(d)-L(d_0)$.

Table VIII shows values for the path loss model parameters. Path loss exponents for the LOS case are less than those for NLOS regions, as expected. Based upon Tx location, the NLOS

exponents also increase with the distance from Tx to the corner (d_1 in Table I). This same dependence on "corner distance" was also observed in [14]. Our measurements are in the smaller range of corner distances covered in [14], but the range of path loss exponents we found generally agrees with values found in [14]. For the LOS case, exponents less than two may indicate waveguiding by the urban canyon walls; this is most noticeable for the 4900 MHz band. For the 700 MHz band LOS results, path loss exponents are generally slightly larger than that for free space (n=2), except for Tx location 3. This location was very close to the building wall on 17th Street, and was partly shadowed by several pillars that extended out from the wall. The NLOS exponents ranged from 3.6 to nearly 6.

C. Frequency Correlation

For wide-sense stationary uncorrelated scattering (WSSUS) channel conditions, the correlation, or coherence bandwidth can be found as the width of the Fourier transform of the average PDP. If we assume this pertains to all measurements, we can find a lower bound for the coherence bandwidth B_z, for which the correlation between channel effects is equal to z [37]: $B_z \geq arccos(z)/(2\pi\sigma_\tau)$, where σ_τ is the RMS-DS. Values of this bandwidth for each case, for a correlation value of z=0.5, appear in Table II, with the minimum coherence bandwidth of approximately 1 MHz occurring for the 4900 MHz NLOS case.

As noted previously though, channel variation due to pedestrian and vehicular motion renders the channel non-stationary after some short time; depending on frequency and velocities, we estimate this to be from as small as 6 ms up to 100 ms or so. Thus, coherence bandwidths should strictly be estimated over times within the channel coherence time. The method in [38] could be used for computing these frequency correlation estimates (FCEs), but unfortunately, we

had only a few (e.g., 2 to 4) transfer functions within any given coherence time, which does not allow for sufficient averaging to yield confident estimates. Figure 11 shows an example FCE for NLOS Tx1-Rx7 pair, computed using all 18 transfer functions—that is, computed over a duration longer than the coherence time. Asymmetry indicates violation of the US condition [38], but the narrow FCE central lobe does tend to corroborate the 1 MHz bandwidth for correlation value 0.5 as estimated via the average PDPs.

IV. Spatial Characteristics

By mounting the transmitter on the two-dimensional positioner described in Section II, we introduced spatial diversity into the measurement system which enabled generating channel impulse responses both as functions of delay τ and angle-of-departure θ. To this end, the measured frequency responses $H_{xy}(f,t_i)$ at grid point (*x*,*y*) on the Cartesian plane of the positioner were synthesized through the conventional beamformer for a rectangular grid [39]

$$H(f,\theta,t_i)=\sum_{x=0,0.25,0.5m}\ \sum_{y=0,0.25,0.5m} H_{xy}(f,t_i)e^{-j\frac{2\pi f}{c}(x\cos\theta+y\sin\theta)}, \tag{11}$$

where *c* is the speed of light. Then taking the inverse Fourier transform of $H(f,\theta,t_i)$ yielded the i^{th} 2D-CIR $h(\tau,\theta,t_i)$. The MPCs identified and indexed according to delay τ_{ki} through the procedure in Section III-A were also indexed according to angle θ_{ki}. The latter was accomplished by segmenting the delay axis of the i^{th} 2D-CIR into bins $\left[\frac{\tau_{ki}+\tau_{k-1,i}}{2},\frac{\tau_{ki}+\tau_{k+1,i}}{2}\right)$ and then searching the power angle profile (PAP) of each bin along the angle axis for the angle θ_{ki} at which the maximum peak occurred.

Most researchers conducting joint spatial-temporal analysis [40]-[48] assume independence between the delay and angle domains. In this study we have also found that assumption to be valid in LOS conditions and partially valid in NLOS to within MPC clusters. Together with equations (5)-(8), this allows the power delay-angle profile $P(\tau,\theta)$ and the MPC delay-angle distribution probability density functions $p(\tau,\theta)$ to be separated respectively into their marginal components as

$$P_{LOS}(\tau,\theta) = P_{\tau,LOS}(\tau)P_{\theta,LOS}(\theta) \tag{12}$$

$$P_{NLOS}(\tau,\theta) = P_{\tau,NLOS}(\tau)P_{\theta,NLOS}(\theta) \tag{13}$$

and

$$p_{LOS}(\tau,\theta) = p_{\tau,LOS}(\tau)p_{\theta,LOS}(\theta) \tag{14}$$

$$p_{NLOS,k}(\tau,\theta) = p_{\tau,NLOS}(\tau)p_{\theta,NLOS}(\theta). \tag{15}$$

where k denotes the cluster index in (6).

In order to characterize the power angle profile, the NLOS MPCs were grouped into three clusters based solely on their delay index according to the same clustering rule described in Section III-A. Once clustered, the powers of the MPCs of each cluster were first normalized to a unity sum while their angles were shifted by setting their mean cluster angle to 0. Then the normalized powers vs. the shifted angles from each cluster were superimposed to extract the angle decay constants $c_{1,\theta}$ and $b_{k1,\theta}$ for the following models through a robust fit[3] to the data points:

$$P_{\theta,LOS}(\theta) = \exp(-c_{1,\theta}\,|\,\theta\,|) \tag{16}$$

$$P_{\theta,NLOS,k}(\theta) = \exp(-b_{k1,\theta}\,|\,\theta - \mu_\theta\,|), \tag{17}$$

[3] Robust fitting henceforth denotes the Trust Region method explained in [49].

where $\mu_\theta \sim \mathcal{U}[0,2\pi)$ is a uniformly distributed random variable that represents the mean cluster angle in NLOS conditions. Table IX contains the parameter values. The values show that in general the power fades with a smaller decay constant in both line-of-sight and non-line-of-sight conditions at 4900 MHz compared to 700 MHz due to the increased scattering at higher frequencies. In NLOS, the decay constant of the first cluster is the largest and tends to decrease with cluster index, meaning that the power spreads in angle progressively from the first to the third cluster. The decay constant of the third cluster is close to zero and comparable to those in LOS conditions for which the power is spread almost uniformly around the azimuth angle-of-departure.

Comment [KR1]: Why would the LOS have a uniform azimuth angle of departure? Could you provide a brief explanation for the reader? This seems counterintuitive to me.

The powers of the first and second clusters in NLOS are the most concentrated in angle since the clusters approach from reflected paths which guide the arrivals to the receiver from distinct directions. Conversely the sole cluster in LOS combines paths which are much shorter and concentrated in time (see RMS-DS in Table II) and so whose arrivals have strong and comparable powers respectively. The variance in their angles is due rather to local scattering. This difference between LOS and NLOS was first observed in [42]. Lastly, the third cluster in NLOS combines reflected paths from distant scatterers with faint and comparable powers, and so resembles LOS however on a larger spatial scale.

Comment [T2]: Added paragraph to explain to reader.

As in [40]-[42], we found the probability density functions of the shifted angles to be Laplacian distributed in both LOS and NLOS conditions:

$$p_{\theta,LOS}(\theta) = \frac{1}{2\nu_{\theta,LOS}} \exp\left(-\frac{|\theta|}{\nu_{\theta,LOS}}\right) \tag{18}$$

$$p_{\theta,NLOS,k}(\theta) = \frac{1}{2\nu_{\theta,NLOS,k}} \exp\left(-\frac{|\theta-\mu_\theta|}{\nu_{\theta,NLOS,k}}\right) \quad \text{sc} \tag{19}$$

The scale parameters $v_{\theta LOS}$ and $v_{\theta LOS,k}$ were also found by robust fitting a curve to the histograms of the centered angles given from the clusters in LOS and NLOS conditions, respectively, with a distinct fit for each cluster *k*. The values appear in Table X and confirm the observations noted above for the power angle profile: in non-line-of-sight conditions, the angle distribution of the first cluster is narrower and tends to spread out with cluster index while the scale parameter of the distribution of the third cluster is comparable to line-of-sight conditions. Also, the distributions at 4900 MHz are wider than at 700 MHz due to increased scattering.

Comment [T3]: Added.

Comment [T4]: Changed width to scale parameter.

Comment [KR5]: Why is this? Could you add a sentence interpreting this for the reader.

Note that considering the i^{th} 2D-CIR alone yields only two responses per location pair for i = 1, 2. In order to generate more responses to greater populate the data points in (16)-(19), we generated 16 CIRs per pair by grouping the grid points of the positioner row-wise by index i = 1,2 and then taking the 8 = 2^3 group permutations to generate $H(f,\theta,t_i)$ in (11). The other 8 permutations were given by grouping the grid points column-wise instead. Although a total of 512 = 2^9 permutations would have been possible by taking the points individually rather than row or column-wise, there would have been less variance between the 2D-CIRs. We found that groups of three struck a fair balance between variance and number of responses. As explained in Section II, while each VNA sweep was completed within the coherence time of the channel, the channel did change during the spatial sweep over the positioner grid points, mainly due the passing cars on the streets. As our intention was to capture the salient properties of the fixed environment, i.e., from the primary scatterers consisting of surrounding buildings and streets, we hoped to average out the mobile scatterers by using the permutation method explained above.

Finally we completed our spatial analysis by providing the complementary angle spread statistics to those described in Section II for delay, namely the root-mean square angle spread

(RMS-AS), the angle window $W_{\theta,90}$, which is defined as the space along the angle axis that contains 90% of the 2D-CIR energy of each cluster, and the angle interval $I_{\theta,25}$, which is defined as the space of the 2D-CIR energy of each cluster containing all impulses above 25 dB down from the largest impulse. These quantities are reported in Table II together with the analogous quantities in delay. The angle dispersion statistics again are consistent with our previous observations in that all three quantities are generally larger or significantly larger at 4900 MHz than 700 MHz, meaning a wider angle spread in the former due to increased scattering.

V. Conclusion

In this paper we reported on channel measurements and models for urban ground-based channels in the 700 MHz and 4900 MHz public safety bands. Non-mobile outdoor measurements for link distances up to approximately 100 m were made using a vector network analyzer and omni-directional antennas at height 1.6 m. For propagation path loss, we found path loss exponents to range from 1.3-4.4 for LOS cases, and from 3.6-5.8 for NLOS cases around corners. Delay dispersion statistics are very similar for the two bands, with the 4900 MHz band generally exhibiting slightly larger delay spreads. The 90th percentile values for root-mean square delay spread range from approximately 100 ns for LOS cases at 700 MHz, to 170 ns for NLOS cases at 4900 MHz, with maximum values of delay spread near 300 ns. We estimate that for correlation value 0.5, minimum correlation bandwidths are approximately from 1 MHz to 2.5 MHz for the 700 MHz LOS channel. For our measurement bandwidths of 75 MHz at 700 MHz, and 100 MHz at 4900 MHz, mean values of the number of multipath components are 11 and 17, respectively. The angle dispersion statistics were also found to be similar for the two bands, however we observed in general a wider MPC angle distribution at 4900 MHz than at 700 MHz

due to the increased scattering at higher frequencies. Also, in NLOS the earlier arriving clusters corresponding to the dominant reflected paths are more concentrated in angle compared to the later. The 90th percentile window containing the angle of departure spread for the 700 MHz LOS data is almost half that of the 700 MHz NLOS, 4900 MHz LOS, or 4900 MHz NLOS data, even though the RMS angular spread is within 10 ° for all four conditions. The 90th percentile window containing the angle of departure spread for the 700 MHz LOS data is 124° and increases to 205^{o}, 209^{o}, and 260^{o} for 700 MHz NLOS, 4900 MHz LOS, and 4900 MHz NLOS respectively, even though the RMS angular spread is within 10° for all four conditions.

Comment [T6]: Added.

Comment [T7]: Changed arrival to departure.

Comment [KR8]: I think it is important to provide a little more of a summary on these data because so many people are interested in this aspect.

Comment [T9]: Should be erased.

Acknowledgement

For their assistance in measurements and analysis, the authors would like to thank Dr. William Young of Sandia National Laboratories, and from NIST, Galen Koepke, Chriss Grosvenor, Jason Coder, and Nada Golmie. This work was funded by the NIST Public Safety Communications Research Laboratory within the NIST Office of Law Enforcement Standards, Dereck Orr, Program Manager.

References

[1] T. L. Doumi, "Spectrum Considerations for Public Safety in the United States," *IEEE Comm. Mag*., vol. 44, no. 1, pp. 30-37, January 2006.

[2] K. Balachandran, K. C. Budka, T. P. Chu, T. L. Doumi, J. H. Kang, "Mobile Responder Communication Networks for Public Safety," *IEEE Comm. Mag*., vol. 44, no. 1, pp. 56-64, January 2006.

[3] TIA, "TIA-902.BAAB-A Wideband Air Interface Scalable Adaptive Modulation (SAM) Physical Layer Specification – Public Safety Wideband Data Standards Project – Digital Radio Technical Standards," Sept. 2003, www.tiaonline.org.

[4] IEEE 802 standards web site, http://standards.ieee.org/getieee802/portfolio.html, July 2009.

[5] J. D. Parsons, *The Mobile Radio Propagation Channel*, 2nd ed., John Wiley & Sons, New York, NY, 2000.

[6] A. F. Molisch, *Wireless Communications*, John Wiley & Sons, New York, NY, 2005.

[7] C. L. Holloway, G. Koepke, D. Camell, K. A. Remley, S. A. Schima, M. McKinley, R. T. Johnk, "Propagation and Detection of Radio Signals Before, During, and After the Implosion of a Large Convention Center," *NIST Technical Note 1542*, June 2006.

[8] C. L. Holloway, W. F. Young, G. Koepke, K. A. Remley, D. Camell, Y. Becquet," Attenuation of Radio Wave Signals Coupled into Twelve Large Building Structures," *NIST Technical Note 1545*, February 2008.

[9] K. A. Remley, G. Koepke, C. L. Holloway, C. Grosvenor, D. Camell, J. Ladbury, D. Novotny, W. F. Young, G. Hough, M. D. McKinley, Y. Becquet, J. Korsnes, "Measurements to Support Broadband Modulated-Signal Transmissions for the Public-Safety Sector," *NIST Technical Note 1546*, April 2008.

[10] E. S. Sousa, V. M. Jovanovic, C. Daigneault, "Delay Spread Measurements for the Digital Cellular Channel in Toronto," *IEEE Trans. Veh. Tech.*, vol. 43, no. 4, pp. 837-847, Nov. 1994.

[11] G. Calcev, et. al., "A Wideband Spatial Channel Model for System-Wide Simulations," *IEEE Trans. Veh. Tech.*, vol. 56, no. 2, pp. 389-403, March 2007.

[12] A. A. M. Saleh, R. A. Valenzuela, "A Statistical Model for Indoor Multipath Propagation," *IEEE Journ. Selected Areas Comm*., vol. SAC-5, no. 2, pp. 128-137, February 1987.

[13] D. W. Matolak, "Channel Modeling for Vehicle-to-Vehicle Communications," *IEEE Communications Magazine,* vol. 46, no. 5, pp. 76-83, May 2008.

[14] J. R. Hampton, N. M. Merheb, W. L. Lain, D. E. Paunil, R. M. Shuford, W. T. Kasch, "Urban Propagation Measurements for Ground Based Communication in the Military UHF Band," *IEEE Trans. Ant. Prop.*, vol. 54, no. 2, pp. 644-654, February 2006.

[15] M. H. Tsai, Y. Lee, "SER and Optimal Power Allocation for DF Cooperative Communications over Nakagami-*m* Fading Channels," *Proc. IEEE Spring Veh. Tech. Conf*., Singapore, 11-14 May 2008.

[16] A. S. Ibrahim, A. K. Sadek, W. Su, K. J. R. Liu, "Cooperative Communications with Partial Channel State Information: When to Cooperate?" *Proc. Globecom '05*, St. Louis, MO, 28 Nov.-2 Dec. 2005.

[17] P. Angueira, M. M. Vélez, D. de la Vega, G. Prieto, D. Guerra, J. M. Matías, J. L. Ordiales, "DTV Reception Quality Field Tests for Portable Outdoor Reception in a Single Frequency Network," *IEEE Trans. Broadcasting*, vol. 50, no. 1, pp. 42-48, March. 2004.

[18] A. Semmar, J.-Y. Chouinard, V. H. Pham, X. Wang, Y. Wu, S. Laflèche, "Digital Broadcasting Television Channel Measurements and Characterization for SIMO Mobile Reception," *IEEE Trans. Broadcasting*, vol. 52, no. 4, pp. 450-463, December 2006.
[19] X. Zhao, J. Kivinen, P. Vainikainen, and K. Skog, "Propagation Characteristics for Wideband Outdoor Mobile Communications at 5.3 GHz," *IEEE J. Sel. Areas Comm.*, vol. 20, no. 3, pp. 507–514, Apr. 2002.
[20] D. W. Matolak, I. Sen, W. Xiong, "The 5-GHz Airport Surface Area Channel—Part I: Measurement and Modeling Results for Large Airports," *IEEE Trans. Veh. Tech.,* vol. 57, no. 4, pp. 2014-2026, July 2008.
[21] A. Chehri, P. Fortier, P. M. Tardif, "Frequency Domain Analysis of UWB Channel Propagation in Underground Mines," *Proc. IEEE Fall Veh. Tech. Conf.*, Montreal, CA, 25-28 September 2006.
[22] T. M. Cover, J. Thomas, *Elements of Information Theory*, 2nd ed., John Wiley & Sons, New York, NY, 1991.
[23] International Telecommunications Union (ITU), "Multipath Propagation and Parameterization of its Characteristics," *Rec. ITU-R P.1407*.
[24] L. J. Greenstein, V. Erceg, Y. S. Yeh, M. V. Clark, "A New Path-Gain/Delay-Spread Propagation Model for Digital Cellular Channels," *IEEE Trans. Comm*., vol. 46, no. 2, pp. 477-485, May 1997.
[25] P. Papazian, "Basic Transmission Loss and Delay Spread Measurements for Frequencies Between 430 and 5750 MHz," *IEEE Trans. Ant. Prop*., vol. 53, no. 2, pp. 694-701, February 2005.
[26] R. J. C. Bultitude, T. C. W. Schenk, N. A. A. Op den Kamp, N. Adnani, "A Propagation-Measurement-Based Evaluation of Channel Characteristics and Models Pertinent to the Expansion of Mobile Radio Systems to Frequencies Beyond 2 GHz," *IEEE Trans. Veh. Tech*., vol. 56, no. 2, pp. 382-388, March 2007.
[27] A. F. Molisch, M. Steinbauer, "Condensed Parameters for Characterizing Wideband Mobile Radio Channels," *Int. Journ. Wireless Inf. Networks,* vol. 6, no. 3, pp. 133-154, 1999.
[28] M. Patzold, *Mobile Fading Channels*, John Wiley & Sons, New York, NY, 2002.
[29] X. Li, K. Pahlavan, "Super-Resolution TOA Estimation with Diversity for Indoor Geolocation," *IEEE Trans. Wireless Comm*., vol. 3, no. 1, pp. 224-234, January 2004.
[30] M. Wax, T. Kailath, "Detection of Signals by Information Theoretic Criteria," *IEEE Trans. Acoust., Speech, Signal Processing*, vol. ASSP-33, pp. 387-392, April 1985.
[31] H. Asplund, A. A. Glazunov, A. F. Molisch, K. I. Pedersen, M. Steinbauer, "The COST 259 Directional Channel Model—Part II: Macrocells," *IEEE Trans. Wireless Comm*., vol. 5, no. 12, pp. 3434-3450, December 2006.
[32] 3rd Generation Partnership Project (3GPP), "3GPP deployment aspects," Valbonne, France, Tech. Rep. TR 25.943 V5.1.0, Jun. 2002.
[33] A. F. Molisch, "Ultrawideband Propagation Channels-Theory, Measurement, and Modeling," *IEEE Trans. Veh. Tech*., vol. 54, no. 5, pp. 1528-1545, September 2005.
[34] R. Kattenbach, "Statistical Distribution of Path Interarrival Times in Indoor Environment," *Proc. Spring IEEE Veh. Tech. Conf*., Ottawa, Canada, pp. 548-551, 18-21 May 1998.
[35] P. Yegani, C.D. McGillem, "A Statistical Model for the Factory Radio Channel," *IEEE Trans. Comm*., vol. 39, no. 10, pp. 1445-1454, Oct. 1991.
[36] A. Papoulis and U. Pillai, *Probability, Random Variables, and Stochastic Processes*, 4th ed. New York: McGraw-Hill, 2001.

[37] B. H. Fleury, “An Uncertainty Relation for WSS Processes and its Application to WSSUS Systems, *IEEE Trans. Comm.*, vol. 44, no. 12, pp. 1632-1634, December 1996.
[38] R. J. C. Bultitude, “Estimating Frequency Correlation Functions from Propagation Measurements on Fading Channels: A Critical Review,” *IEEE Journ. Selected Areas Comm.*, vol. 20, no. 6, pp. 1133-1143, August 2002.
[39] M. Uthansakul and M.E. Bialkowski, “Wideband Beam Forming with a Rectangular Array Antenna,” *IEEE European Conf. on Wireless Technology*, pp. 63-66, Oct. 2005.
[40] Q. H. Spencer, B. D. Jeffs, M. A. Jensen, A. L. Swindlehurst, “Modeling the Statistical Time and Angle of Arrival Characteristics of an Indoor Multipath Channel,” *IEEE Journ. Selected Areas Comm.*, vol. 18, no. 3, pp. 347-360, March 2000.
[41] R. J.-M. Cramer, R. A. Scholtz, M. Z. Win, “Evaluation of an Ultra-Wide-Band Propagation Channel,” *IEEE Trans. Antennas and Propagation*, vol. 50, no. 5, pp. 561-570, May 2002.
[42] C.-C. Chong, C.-M. Tan, D. I. Laurenson, S. McLaughlin, M. A. Beach, A. R. Nix, “A New Statistical Wideband Spatio-Temporal Channel Model for 5-GHz Band WLAN Systems,” *IEEE Journ. Selected Areas Comm.*, vol. 21, no. 2, pp. 139-149, Feb. 2003.
[43] K. Haneda, J.-I. Takada, T. Kobayashi, “Cluster Properties Investigated From a Series of Ultrawideband Double Directional Propagation Measurements in Home Environments,” *IEEE Trans. Antennas and Propagation*, vol. 54, no. 12, pp. 3778-3788, Dec. 2006.
[44] N. Czink, X. Yin, H. Ozcelik, M. Herdin, E. Bonek, B. H. Fleury, “Cluster Characteristics in a MIMO Indoor Propagation Environment," *IEEE Trans. Wireless Communications*, vol. 6, no. 4, pp. 1465-1475, April 2007.
[45] J. Medbo, J.-E. Berg, “Spatio-Temporal Channel Characteristics at 5 GHz in a Typical Office Environment,” *IEEE Vehicular Tech. Conf., Fall*, pp. 1256-1260, October 2001.
[46] K. Yu, Q. Li, D. Cheung, C. Prettie, “On the Tap and Cluster Angular Spreads of Indoor WLAN Channels,” *IEEE Vehicular Tech. Conf., Spring*, pp. 218-222, May 2003.
[47] A. S. Y. Poon, M. Ho, “Indoor Multiple-Antenna Channel Characterization from 2 to 8 GHz,” *IEEE Int. Conf. Communications*, May 2003.
[48] S. Venkatesh, V. Bharadwaj, R. M. Buehrer, “A New Spatial Model for Impulse-Based Ultra-Wideband Channels,” *IEEE Vehicular Tech. Conf., Fall*, Sept. 2005.
[49] M. A. Branch, T. F. Coleman, Y. Li, “A Subspace, Interior, and Conjugate Gradient Method for Large-Scale Bound-Constrained Minimization Problems,” *SIAM Journal Scientific Computing*, vol. 21, no. 1, pp. 1-23, 1999.

Figure 1. Left: Google map view of test area in downtown Denver. Transmit locations denoted T, receiver locations denoted R. Right: photo of Rx antennas at location R5.

TABLE I. Transmitter (Tx) to Receiver (Rx) distances (m). LOS links contain only one distance (*d*), and NLOS links contain either two (d_1, d_2) for L-shaped paths, or three (d_1, d_2, d_3) for U-shaped paths.

	Rx2	**Rx3**	**Rx4**	**Rx5**	**Rx6**	**Rx7**	**Rx8**	**Rx9**	**Rx10**	**Rx11**	**Rx12**
Tx1	d=10	d=20	d=30	d=40	d_1=40 d_2=10	d_1=40 d_2=20	d_1=40 d_2=30	d_1=40 d_2=40	d_1=40 d_2=43 d_3=13	d_1=40 d_2=5.5	d_1=40 d_2=35.5
Tx2	d=50	d=60	d=70	d=80	d_1=80 d_2=10	d_1=80 d_2=20	d_1=80 d_2=30	d_1=80 d_2=40	d_1=80 d_2=43 d_3=13	d=5.5	d=35.5
Tx3	d=36	d=46	d=56	d=66	d_1=66 d_2=10	d_1=66 d_2=20	d_1=66 d_2=30	d_1=66 d_2=40	d_1=66 d_2=43 d_3=13	d_1=14 d_2=5.5	d_1=14 d_2=35.5

Figure 2. Illustration of VNA test configuration.

Figure 3. Plan view diagram of antenna positioner, showing nine positions.

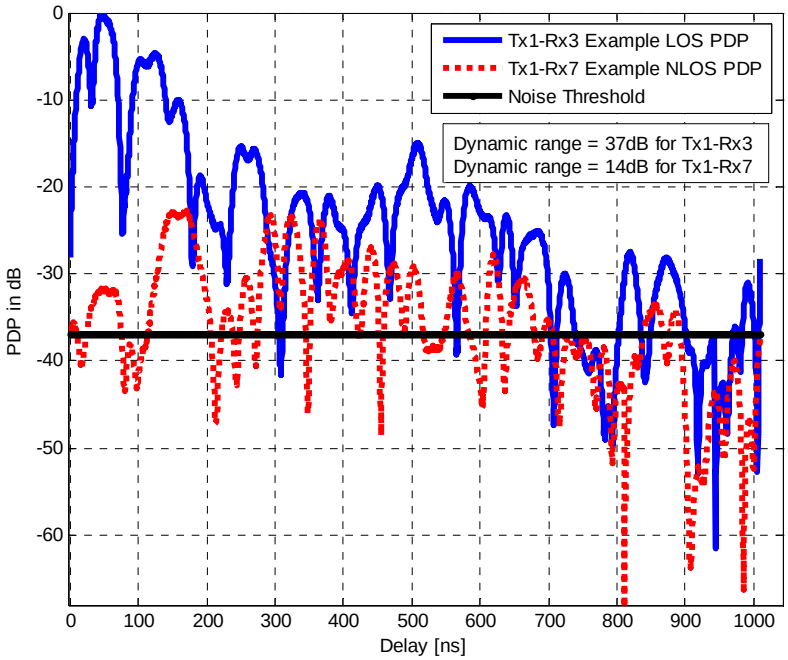

Figure 4. Example PDPs for LOS (Tx1-Rx3) and NLOS (Tx1-Rx7) locations, 700 MHz band.

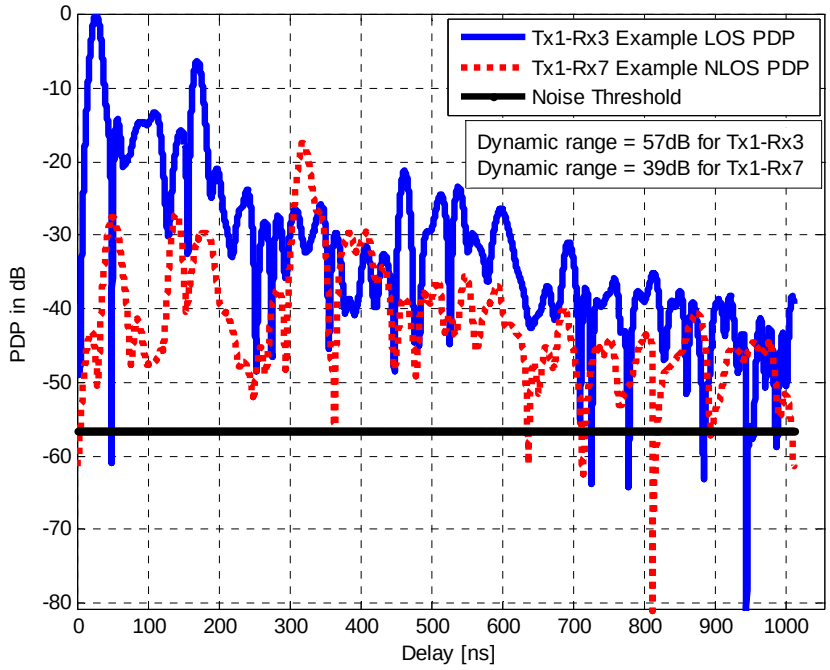

Figure 5. Example PDPs for LOS (Tx1-Rx3) and NLOS (Tx1-Rx7) locations, 4900 MHz band.

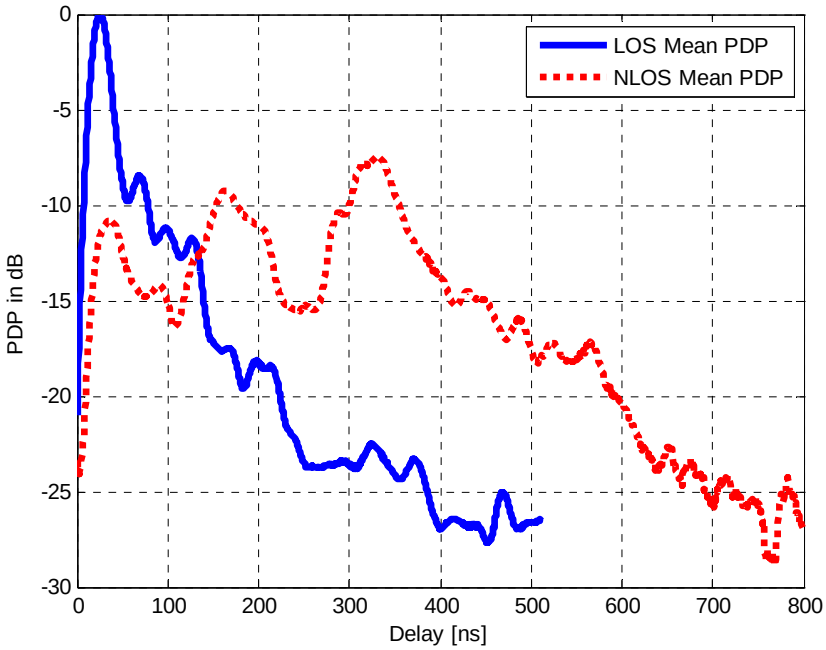

Figure 6. Average PDPs for all LOS and NLOS locations, 700 MHz band.

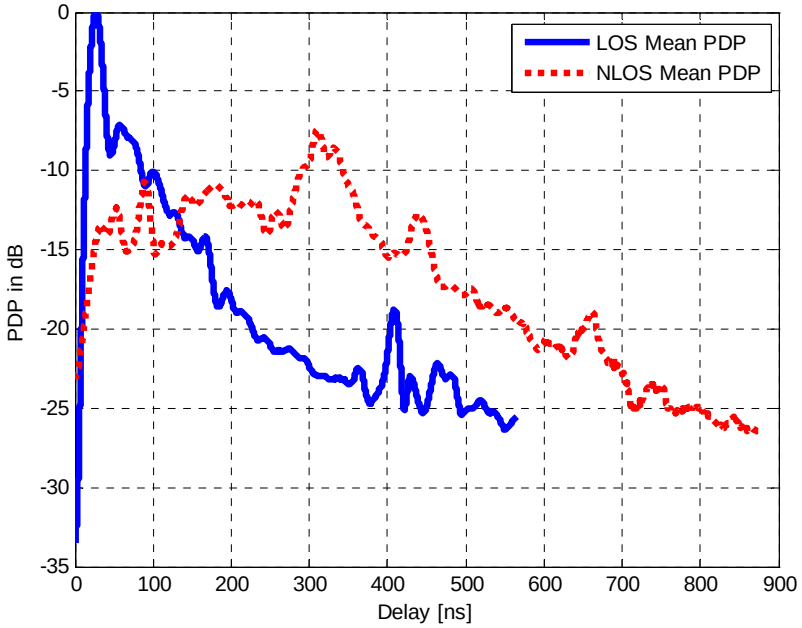

Figure 7. Average PDPs for all LOS and NLOS locations, 4900 MHz band.

TABLE II. Summary delay and angle spread statistics, plus minimum coherence bandwidth estimates for 0.5 correlation, $B_{0.5}$ (MHz).

Condition (band)	**RMS-DS**	**RMS-AS**	$\mathbf{W_{\tau,90}}$	$\mathbf{W_{\theta,90}}$	$\mathbf{I_{\tau,25}}$	$\mathbf{I_{\theta,25}}$	$B_{0.5}$
LOS (700)	66	98	166	124	386	242	2.52
LOS (4900)	87	103	235	205	519	279	1.92
NLOS (700)	147	107	501	209	798	288	1.33
NLOS (4900)	156	97	528	260	875	292	1.07

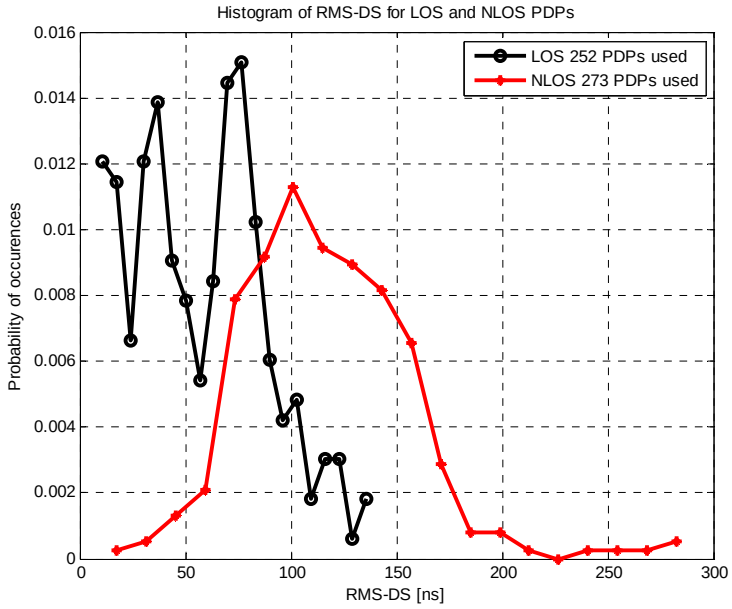

Figure 8. Histograms for RMS-DS for PDPs in both LOS and NLOS locations, 700 MHz band.

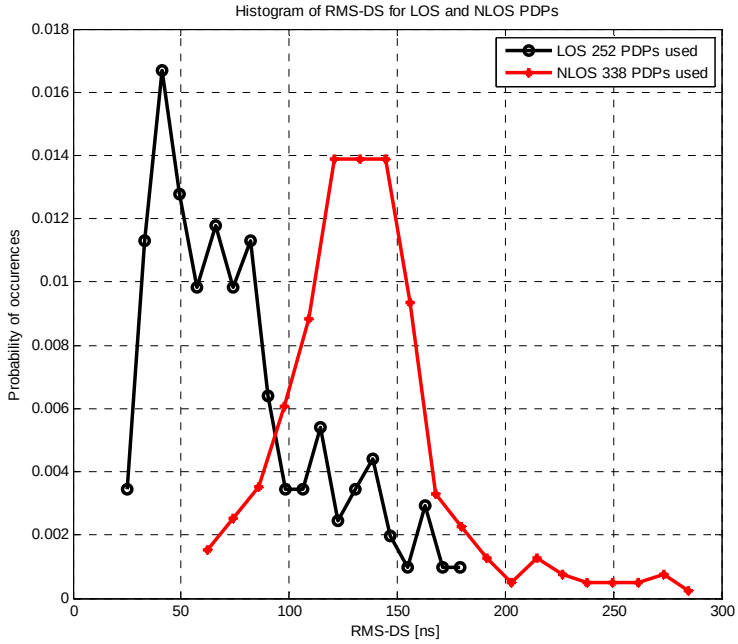

Figure 9. Histograms for RMS-DS for PDPs in both LOS and NLOS locations, 4900 MHz band.

TABLE III. Summary instantaneous RMS-DS statistics (ns).

Condition (band)	Min	Mean	Median	90th Percentile	Max	Standard Deviation
LOS (700)	7	57	56	98	139	32
LOS (4900)	21	75	66	134	183	37
NLOS (700)	11	116	114	163	290	40
NLOS (4900)	57	135	131	172	291	37

TABLE IV. 90% delay window W_{90} and 25 dB delay interval I_{25} statistics (ns).

Condition (band)	Min	Mean	Median	Max
LOS W_{90} (700)	24	152	133	427
LOS W_{90} (4900)	33	205	157	538
LOS I_{25} (700)	42	384	435	746
LOS I_{25} (4900)	112	466	469	970
NLOS W_{90} (700)	36	377	370	976
NLOS W_{90} (4900)	157	442	437	984
NLOS I_{25} (700)	51	645	671	1000
NLOS I_{25} (4900)	355	791	825	1000

TABLE V. Statistics for number of multipath components L_p, using a 25 dB threshold from PDP peak, plus modified uniform probability mass function fit parameter p_0.

L_p Statistic	700 MHz		4900 MHz	
	LOS	NLOS	LOS	NLOS
Minimum	4	3	3	3
Median	11.50	13	17	20.50
Mean	10.49	11.47	16	17.91
90th Percentile	14	14	21	21
Maximum	14	14	21	21
Standard Deviation	3.34	3.10	4.70	4.74
p_0	0.3294	0.4428	0.2619	0.5

TABLE VI. PDP exponential fit parameters of equations (5), (6).

Parameter	700 MHz	4900 MHz
c_0	1.09	0.98
c_1	0.07	0.076
b_{10}	0.39	0.27
b_{11}	0.017	0.003
b_{20}	6.56	0.56
b_{21}	0.018	0.003
τ_2 (ns)	73	70
b_{30}	129	26.7

b_{31}	0.017	0.013
τ_3 (ns)	215	218

TABLE VII. MPC delay distribution probability density function parameters, equations (7), (8).

Band	**LOS Parameter v**	**NLOS Parameters (a,b)**
700 MHz	318.2	(452.7, 1.57)
4900 MHz	340.6	(472.8, 1.6)

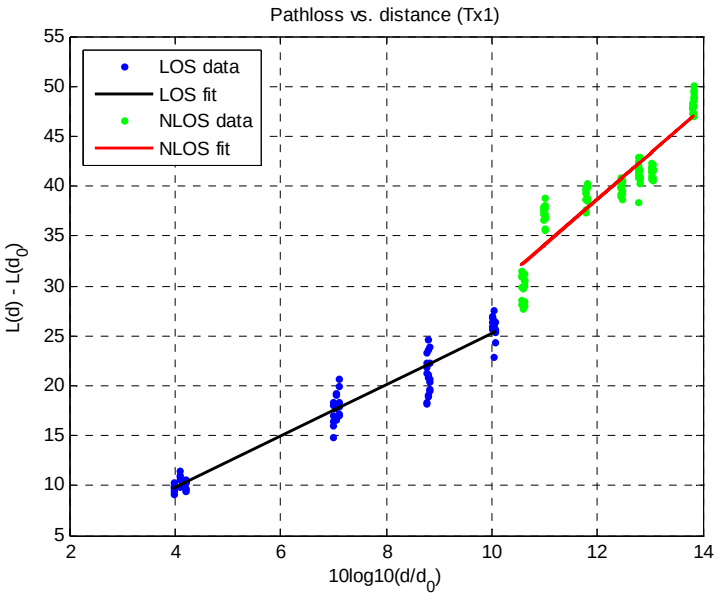

Figure 10. Excess propagation path loss (dB) vs. *log(distance/d_0)*, 700 MHz band.

TABLE VIII. Path loss model parameters: *n*=path loss exponent, σ_X=standard deviation of Gaussian RV, L_c = corner loss.

		n	**σ_X (dB)**	**L_c (dB)**
700 MHz				
Tx1	**LOS**	2.57	1.46	4.23
	NLOS	4.57	2.13	
Tx2	**LOS**	2.34	2.94	8.27
	NLOS	5.76	2.23	
Tx3	**LOS**	4.37	2.63	11.69
	NLOS	3.42	3.44	

All Tx	**LOS**	2.27	3.06	
	NLOS	3.58	2.92	
4900 MHz				
Tx1	**LOS**	1.34	1.25	7.73
	NLOS	4.04	2.47	
Tx2	**LOS**	1.59	2.54	7.08
	NLOS	5.18	3.23	
Tx3	**LOS**	1.53	2.74	12.87
	NLOS	3.47	3.02	
All Tx	**LOS**	1.64	2.65	
	NLOS	3.35	3.16	

Figure 11. Example NLOS frequency correlation estimate for Tx1-Rx7 location pair.

TABLE IX. PAP exponential fit parameters of equations (16), (17).

Parameter	**700 MHz** ($1/^{o}$)	**4900 MHz** ($1/^{o}$)
$\mathbf{c_{1,\theta}}$	0.00103	0.00040
$\mathbf{b_{11,\theta}}$	0.00494	0.00257
$\mathbf{b_{21,\theta}}$	0.00221	0.00012
$\mathbf{b_{31,\theta}}$	0.00124	0.00040

TABLE X. MPC angle distribution probability density function parameters, equations (18), (19).

Parameter	**700 MHz** (^{0})	**4900 MHz** (^{0})
$\mathbf{\nu_{LOS}}$	73.8	86.3
$\mathbf{\nu_{NLOS,1}}$	52.7	56.6
$\mathbf{\nu_{NLOS,2}}$	40.3	81.9
$\mathbf{\nu_{NLOS,3}}$	77.3	86.0